ELSEVIER

Physics of the Earth and Planetary Interiors 127 (2001) 67–81

PHYSICS OF THE EARTH AND PLANETARY INTERIORS

www.elsevier.com/locate/pepi

Subduction zone rheology☆

Donald J. Weidner*, Jiuhua Chen, Yaqin Xu, Yujun Wu, Michael T. Vaughan, Li Li

CHiPR and Department of Geosciences, State University of New York, Stony Brook, NY 11794-2100, USA

Received 17 March 2000; accepted 5 November 2000

Abstract

Rheological flow laws can be obtained from studies using multi-anvil high-pressure systems with synchrotron-based piezometers and strain metrics. The high flux X-ray source provides minute-scale time resolution with accurate measurement of diffraction patterns and direct sample images. Measurements of length changes with an accuracy of one part in 10^4 are being developed and will provide a new generation of rheological tools. Flow laws derived from peak broadening agree well with literature data for corundum, spinel, and olivine.

Properties of several mantle phases are compared for the temperature and pressure regime appropriate to a subducting slab. Temperature dependence of these properties exhibits a strong, temperature insensitive low temperature region, a thermally softened region and a weak high temperature region. The middle of these could be related to the seismogenic zone of a subduction zone. The progression of the temperature for softening with mineral phase suggests that earthquakes deeper than 400 km correspond to higher temperatures than for olivine in the upper 400 km. Plastic instabilities are suggested by these data as the origin of deep earthquakes.

Keywords: Rheology; Mantle minerals; Subduction zone; Deep earthquakes; Strength; Synchrotron; Stress measurements; Olivine; Wadsleyite; Ringwoodite; Perovskite; Majorite

1. Introduction

Subduction zones are unique regions of the earth's mantle as evidenced by the large lateral variations in seismic velocity and high level of seismicity. Indeed the low temperatures expected in such regions provide the basis for the distinction from 'normal mantle'. The rheology of the materials in subduction zones dictates many of the dynamic processes that occur in this region. Deformation of the subducting slab must occur by means of plastic deformation. Earthquakes sample the rheology of the region. The material must be strong enough to hold significant stress over time, yet capable of catastrophic stress release in these earthquakes. While the instability may be associated with dehydration, phase transformation, or plastic shear instability, the rheology of the material significantly influences the process. Plastic processes in a low-temperature, high-stress, high-pressure environment for the mantle suite of minerals have not yet been studied owing to experimental limitations. New advances in synchrotron X-ray studies at high pressure offer in situ piezometers and strain metrics that allow the determination of flow laws in the pressure and temperature regime of a subducting slab for both low- and high-pressure phases. Here, we examine the current state of development of these tools. We demonstrate that the flow laws determined by these methods agree with those in the literature for a few standard materials and

☆ This is a Mineral Physics Institute publication # MPI-276.

* Corresponding author. Fax: +1-631-632-8140.

E-mail address: donald.weidner@sunysb.edu (D.J. Weidner).

0031-9201/01/$ – see front matter
PII: S0031-9201(01)00222-9

provide preliminary results for the major minerals of the mantle.

2. Experimental

In this study, we use a multi-anvil high-pressure apparatus to create pressures up to 20 GPa and deviatoric stress in the sample along with synchrotron generated X-rays to characterize the stress–strain field in the sample. Temperature is increased up to 1500°C during the experiment with special attention to the temperature range appropriate to the subducting slab. Yield is determined if the stress that is supported by the sample saturates during loading (i.e. no longer elastic) and decreases with heating as the strength is reduced.

It is convenient to distinguish two scales of deviatoric stress relative to the X-ray sampling volume. We use the term macro-scale stress to indicate the deviatoric stress field that is uniform over the sampling volume and micro-scale stress to indicate the stress field that is heterogeneous in this volume. Both stress fields can be exploited to yield rheology information, but will require different experimental protocols as they will have different manifestations in the diffracted X-ray signal and they have different expressions of the plastic strain field. Micro-scale stress broadens the diffraction peak with the resulting plastic strain occurring at the expense of elastic strain of the sample. In this regard, micro-scale deformation experiments are relaxation experiments in that the volume of the sample remains quite constant as the stress relaxes by converting the elastic strain to plastic strain. Samples recovered from different stages of yield have been examined with transmission electron microscopy to determine the deformation mechanism. Time resolution of the relaxation process has been quantified and the results interpreted in terms of flow laws. To date, the observations are in good agreement with existing data. In the case of macro-scale stress, a uniform deviatoric stress is generated over the entire sample by appropriate design of the cell assembly. The magnitude of stress can be determined by quantifying the strains recorded by the individual diffraction lines, while strain is monitored using direct images of the sample with X-ray shadowgraphs. Time resolution allows definition of the stress–strain rate relation.

2.1. High-pressure apparatus

We use two multi-anvil high-pressure toolings with a 250 ton press (SAM-85) on the superconducting beam line (X-17) of the National Synchrotron Light Source (NSLS) and at the GSECARS beamline at the Advanced Light Source. The DIA cubic anvil system is described by Weidner et al. (1992a,b), but we will describe a few of the salient features here. With this system, the force of a uniaxial ram is transmitted to six anvils that simultaneously advance into the solid pressure medium that is cubic in shape. Gaps between the anvils of about 0.5 mm afford space for X-rays to enter the sample chamber and diffracted X-rays to exit. The cross-section of the pressure medium is illustrated in Fig. 1. A cylindrical hole in the sample chamber contains a graphite furnace and the sample. The dimension of the sample volume is about 1 mm in diameter and 1.5 mm long. A thermocouple that passes through one of the anvil gaps monitors the temperature. A diffraction standard with a well-known equation of state is used to define the pressure. With 4 mm truncated, tapered anvils this system operates routinely to 10 GPa and on occasion to 13 GPa.

The second tooling, the T-cup, is a 6–8 style system using 10 mm cubes for the second stage (Vaughan et al., 1998). Pressures to 23 GPa have been achieved with tungsten carbide anvils. The general operation of both pressure cells is similar with comparable X-ray optics. Together they afford the possibility of exploring the rheological properties to pressures in excess of 20 GPa and temperatures up to 1500°C.

White X-radiation yields an energy dispersive analysis with energies between 15 and 100 keV. We typically use a 2θ angle of 5–10°. Data gathering times as short as 30 s from an X-ray beam of dimensions of 100 μm × 100 μm provide robust X-ray patterns that can be analyzed for position and width. The accuracy of the lattice spacing determinations is often 0.00008 nm. This rapid mode of data acquisition enables analysis of the evolution of the stress–strain rate relationship during fast relaxation of the stress.

Monochromatic radiation at selectable energies up to 80 keV can be used with an imaging plate recording system or with a charge coupled device (CCD) recording system. Monochromatic radiation offers an increase peak-width resolution of about a factor of 4

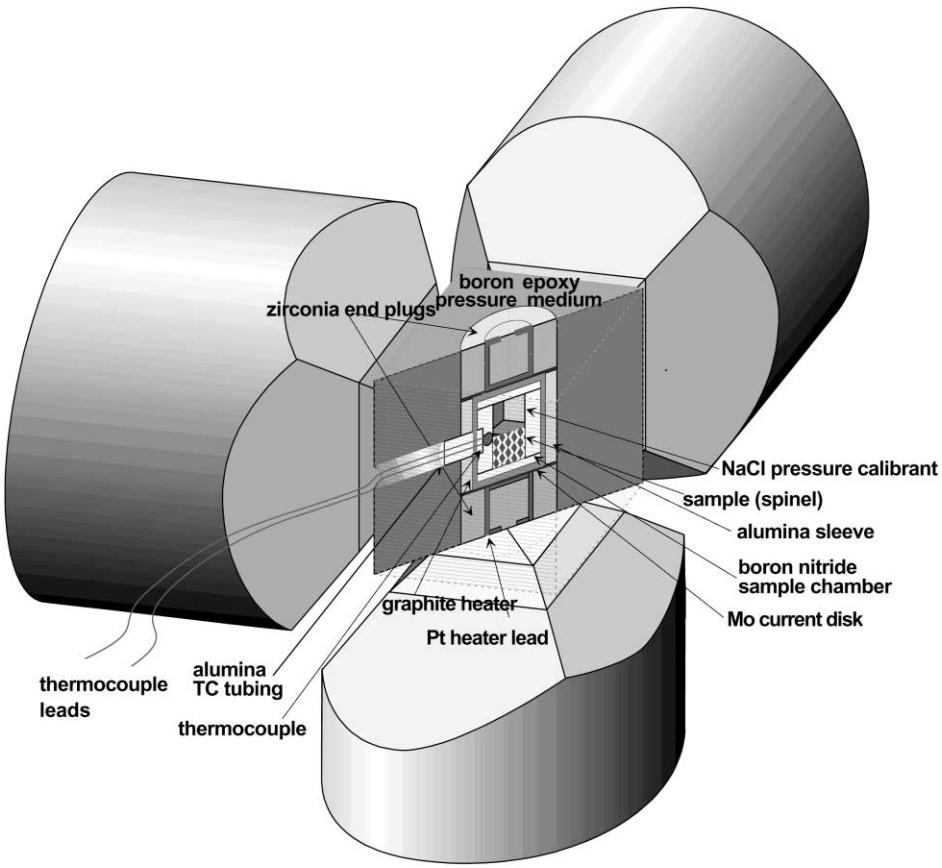

Fig. 1. Cross-section of pressure cell for cubic DIA apparatus.

over the white radiation, but at a cost in time resolution of about a factor of 6.

By analyzing the lattice parameters of samples at several vertical positions within the sample chamber, we have determined that the temperature variation over the entire sample length is of the order of 20 at 1200°C. Using multiple thermocouples, we find that the radial temperature gradient is less than 5°C at these conditions. We find no evidence of a vertical pressure gradient at room temperature.

2.2. Micro-scale stress

Deviatoric stress generally accompanies hydrostatic pressure in all high-pressure devices unless each individual grain is surrounded by a fluid medium that has no strength. This stress field can be uniform throughout the sample, with little or no variation from grain to grain, or it can be heterogeneous, varying in magnitude and orientation from point to point as long as mechanical equilibrium is satisfied. Homogeneous stresses arise from anisotropy of the elastic and plastic properties of the pressurizing medium or from the symmetry of the loading system. A heterogeneous stress field results from heterogeneities within the sample such as a two-phase mixture or randomly oriented elastically anisotropic grains. A sample comprised of loosely packed grains will experience deviatoric stresses as it is compressed owing to the void space between grains and the point contacts of the grains. These micro-scale stresses will occur even if the sample is externally loaded hydrostatically.

Our experimental technique using micro-scale stress for rheological measurements is detailed in

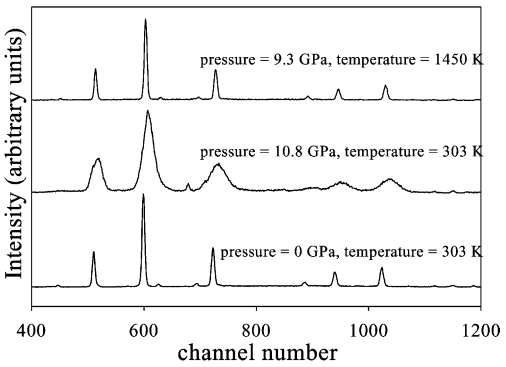

Fig. 2. Diffraction signal from spinel at ambient conditions, at room temperature and 10 GPa, and at 10 GPa and 1450 K. Note the evolution of peak width.

Weidner (1998) and Weidner et al. (1998). We model the manner that the diffraction signal will reflect this stress field. Each diffraction peak is the sum of diffraction from only a subset of grains within the specimen. These are the grains that have the particular orientation that aligns the specific set of lattice planes with the diffraction vector. The micro-scale deviatoric stress field will broaden the X-ray diffraction lines with the amount of line broadening determined by the distribution of longitudinal elastic strain parallel to the diffraction vector. Fig. 2 displays the diffraction signal from $MgAl_2O_4$, spinel at ambient conditions, after the sample was compressed to 10.8 GPa at room temperature, and after it was heated to 1450 K at this pressure. The amount of broadening of the peaks on compression reflects the magnitude of the elastically supported deviatoric stress. On heating, the sample weakens, the amount of deviatoric stress that can be supported reduces, and the peaks narrow. During this process, the total sample-strain remains constant, with elastic strain being relieved by plastic strain. Thus, the amount of peak broadening yields the magnitude of the deviatoric stress and the amount of narrowing with time or temperature reflects the plastic strain. Differentiating the plastic strain with time yields strain rate.

Weidner (1998) and Weidner et al. (1998) demonstrate the effects of sample grain size and elastic anisotropy on peak shapes and how these can be removed from the strain signal. Strain broadening results from stresses generated by forces at the surface of the grain as well as dislocations internal to the grains. Both sources of stress induce dislocation flow as evidenced by the fact that internal strains can be eliminated by annealing at high temperature in the absence of applied stress by dislocation mediated processes.

2.2.1. Case studies

2.2.1.1. Spinel. Weidner et al. (1998) report the micro-scale stress evolution of a spinel ($MgAl_2O_4$) sample as shown in Fig. 3. All of these data were taken in a single run in which pressure was first increased to over 10 GPa and the sample was then heated to 400°C where the time evolution of the peak width was monitored. Then the sample was heated to 600°C with continued monitoring of peak width. This procedure was repeated at 800 and 1100°C. On further heating, the peak width was entirely dominated by the instrumental peak width with strain broadening lost in the noise. The stress values in this figure represent the differential stress and are obtained by deconvolving the instrument response from the diffraction peak shape and multiplying by Young's modulus (Weidner et al., 1998). These relaxation experiments contain information about strain rate as well as stress because

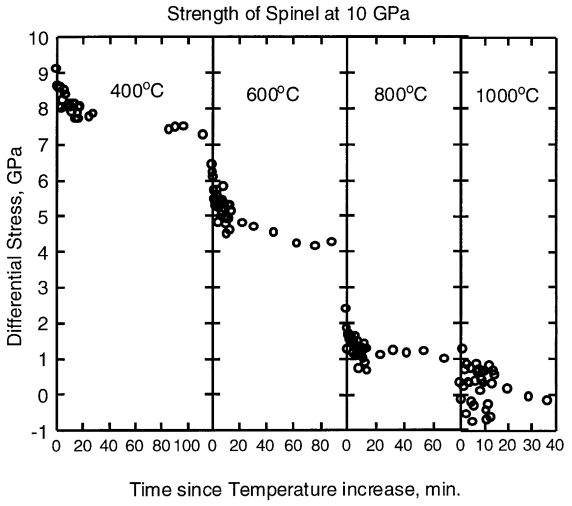

Fig. 3. Differential stress in spinel ($MgAl_2O_4$) as a function of time for a sample compressed to 10 GPa. The sample is heated in steps from room temperature to 1100°C. The heating time is about 1 s; data collection times are about 30 s.

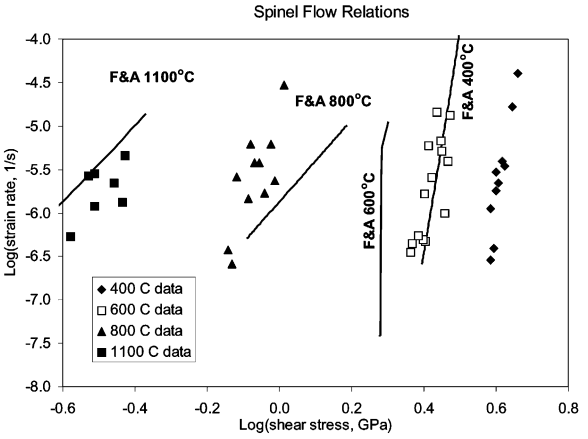

Fig. 4. Stress–strain rate relations for spinel. Observed data are shown by symbols and the experimental temperature is noted. Lines are from the model of Frost and Ashby (1982).

the total sample strain remains constant or

$$\left(\frac{\partial\varepsilon}{\partial t}\right)_{\text{tot}} = \left(\frac{\partial\varepsilon}{\partial t}\right)_{\text{plastic}} + \left(\frac{\partial\varepsilon}{\partial t}\right)_{\text{elastic}} = 0 \qquad (1)$$

Thus, the plastic sample strain rate is equal to the negative of the elastic sample strain rate. Relaxation data, by virtue of this equation, contain information on both strain rate and stress. Only elastic strain is directly observed in the experiment. Stress is deduced from the magnitude of elastic strain and strain rate is defined by the time variation of the elastic strain. For these spinel data, we fit a parametric relation to the elastic strain versus time ($\ln(\varepsilon) = a + b\ln(t)$), and differentiate to obtain strain rate. The resulting shear strain rate versus shear stress is illustrated in Fig. 4. The slopes of the lines yield values, n, which are the effective power for a power law stress strain rate model. This value is generally close to 3 in the region where dislocation recovery is operative and to 1 in the region where diffusion processes dominate. High values suggest that dislocation glide is the deformation mechanism.

The lines shown in Fig. 4 were obtained from the flow law model of Frost and Ashby (1982) for this temperature–stress–strain rate region. Their model has three mechanisms active in this temperature regime. At the lowest temperature and highest stress, their model includes a dislocation glide region where flow is limited by lattice resistance and governed by the rate equation

$$\dot{\varepsilon} = A\left(\frac{\sigma}{\mu}\right)^2 \exp - \left\{\frac{\Delta F}{kT}\left[1 - \left(\frac{\sigma}{\tau}\right)^{3/4}\right]^{4/3}\right\} \qquad (2)$$

where σ is the shear stress, μ the shear modulus, ΔF the activation free energy, and τ is the flow stress at 0 K. According to their model, this relation dominates the flow at temperatures up to 600°C. At 600°C as stress reduces, flow becomes limited by obstacle resistance given by the rate equation

$$\dot{\varepsilon} = A\exp - \left\{\frac{\Delta F}{kT}\left[1 - \left(\frac{\sigma}{\tau}\right)\right]\right\} \qquad (3)$$

At higher temperatures, the obstacles are overcome by recovery processes and the flow law transforms to a power law relation controlled by oxygen diffusion. They derived the parameters for the low temperature region from the hardness data of Westbrook (1966) after some corrections for cracking and for elastic distortion. The power law region is modeled on oxygen diffusion of Ando and Oishi (1974) and constrained by compression tests of Choi (1965). The agreement between our observations and the Frost and Ashby model in Fig. 4 is quite good. Indeed the agreement suggests that our observations, taken in a relaxation mode, reflect the steady state flow law. As with the model, 600–800°C appears to represent a transition from glide to power law creep as reflected by a change in slope of the curves and the increased temperature sensitivity of the flow law. Indeed, the new data can be used to refine the flow parameters used in these models. A change of (τ/μ) from 0.02 to 0.15 for the obstacle parameter and from 0.085 to 0.12 for the lattice resistance brings the model flow law closer to the data as shown in Fig. 5. Such changes are well within the latitude of the data used to constrain the Frost and Ashby (1982) model.

2.2.1.2. Corundum. Fig. 6 illustrates the stress–strain rate relations observed for corundum at 200, 600, 700, and 1200°C from several relaxation experiments in which the temperature was held constant and the time dependence of stress and strain were monitored. These data require a small temperature dependence of strength for temperatures less than

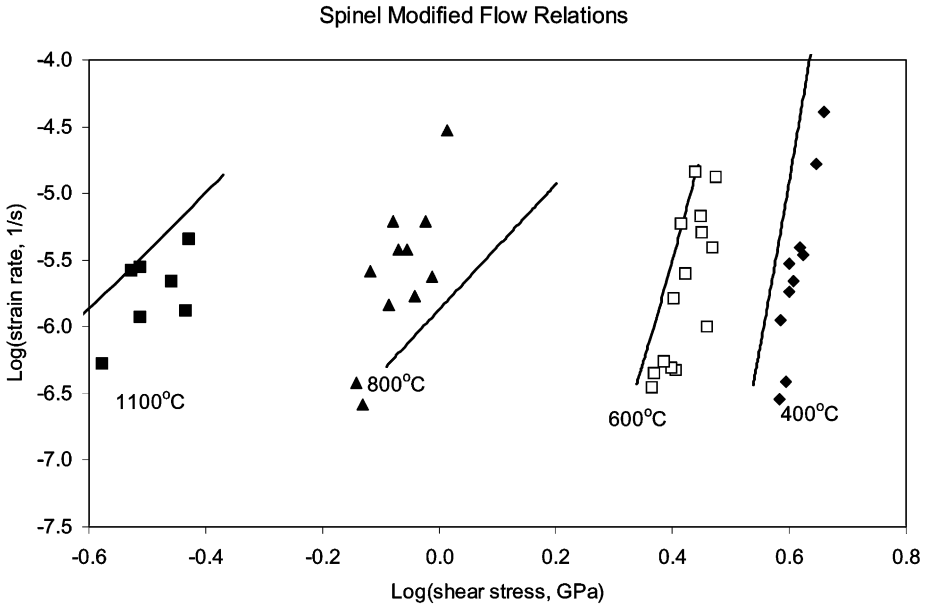

Fig. 5. Stress–strain rate relations for spinel. Observed data are shown by symbols and the experimental temperature is noted. Lines are from the model modified from that of Frost and Ashby (1982) by changing (τ/μ) from 0.02 to 0.15 for the obstacle stress parameter and from 0.085 to 0.12 for the lattice resistance stress parameter.

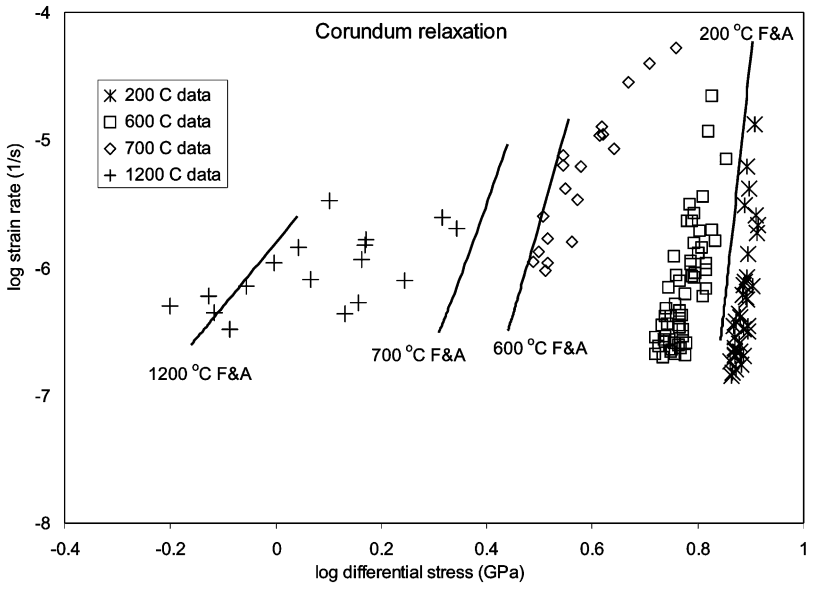

Fig. 6. Stress–strain rate relations for corundum. Observed data are shown by symbols and the experimental temperature is noted. Lines are from the model of Frost and Ashby (1982).

600°C, but a rapid evolution of strength at higher temperatures. The lines in this figure represent the model of Frost and Ashby (1982) for corundum. Their low temperature curves (700°C and less) are based on a lattice resistance controlled glide relation and their high temperature curve is for a power law creep relation controlled by oxygen and aluminum diffusion. In the region where their model has the strongest data control, namely from low temperature indentation experiments and high temperature creep experiments, the model is in excellent agreement with our results. Furthermore, the slopes of the curves are in good agreement with the data, thus, yielding similar stress dependence of the strain rate. The differences between model and data in the dislocation glide region may suggest slight variations in the model parameters. Again the strong agreement between the model and our data suggest that the data are providing a excellent sampling of the flow laws.

2.2.1.3. Olivine. Despite the abundance of studies of the rheology of olivine, there are relatively few in the low temperature regime. Phakey et al. (1972) obtained stress–strain curves for single crystal forsterite at 600 and 800°C under 1 GPa confining pressure. Their test at 800°C with different crystallographic orientations gave yield stresses that ranged from 0.57 to 1.3 GPa. Goetze (1978) and Evans and Goetze (1979) measured indentation hardness to study the strength of olivine up to 800°C. Meade and Jeanloz (1990) studied the room temperature strength of olivine up to 30 GPa with the diamond anvil cell. We have studied olivine in a manner similar to that described above for corundum and spinel. Our room temperature data are in excellent agreement with these previous workers. Fig. 7 presents the differential stress calculated from line broadening as a function of loading pressure for San Carlos olivine. The stress increases rapidly with pressure at low pressure, presumably indicating elastic loading, until it saturates at about 5.5 GPa. With further loading, it increases only moderately, indicating a saturation of stress and hence plastic flow. Room temperature results from Evans and Goetze (1979) and Meade and Jeanloz (1990) are also included in the figure. Their data suggest a slight increase in strength with increasing pressure and are completely consistent with our measurements. Strength as a function of temperature from indentation experiments of Evans and

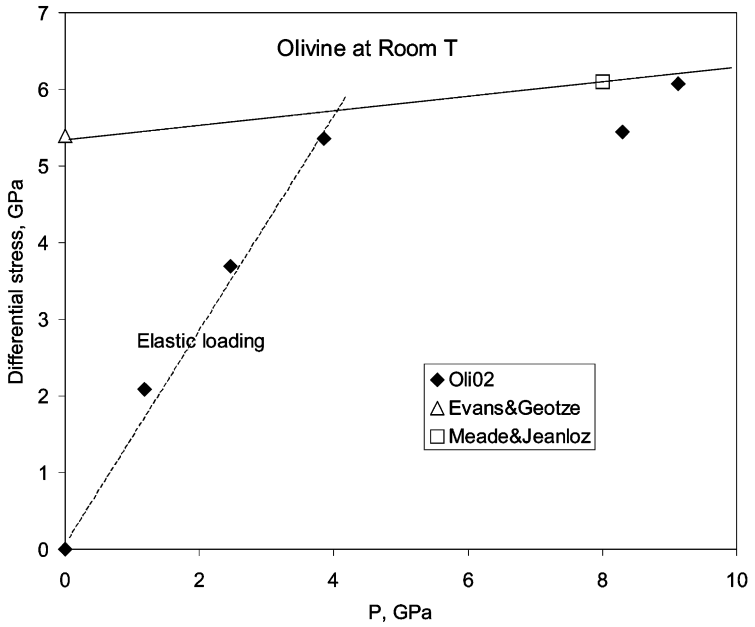

Fig. 7. Differential stress in San Carlos olivine as a function of pressure. Data from this study are compared with that of Evans and Goetze (1979) at room pressure and Meade and Jeanloz (1990) at elevated pressure.

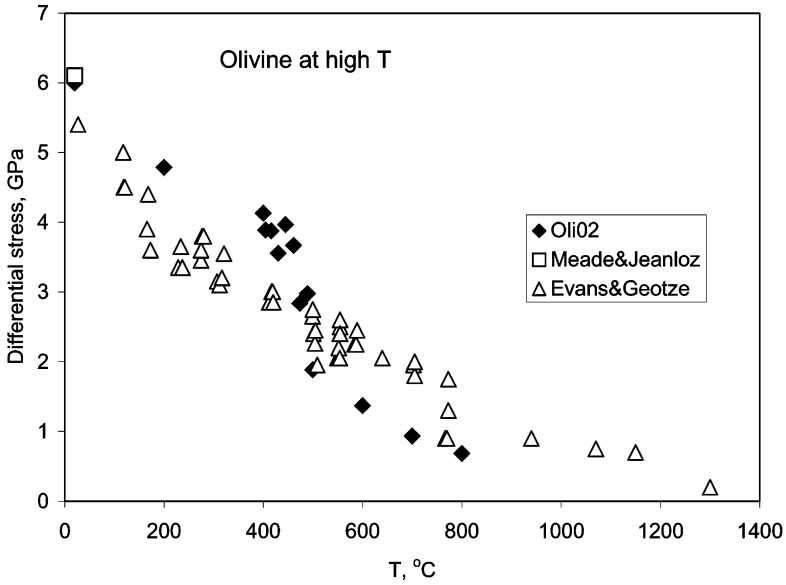

Fig. 8. Differential stress as a function of temperature. Data correspond to the stress after 1000 s and are compared with data of Evans and Goetze (1979) that was collected at room pressure using indentation techniques.

Goetze (1979) is compared with our data in Fig. 8. Our data correspond to strength at temperature measured about 1000 s after relaxation at that temperature has begun. The sample will usually have a strain rate of about $10^{-7}\,s^{-1}$ at this time. Our stresses are slightly larger than that of Evans and Goetze (1979) in the low temperature regime ($T < 500^{\circ}C$) as expected from the pressure effect indicated in Fig. 7. At higher temperatures, our strength is lower than their values, suggesting a change in the flow mechanism. Nonetheless, it is clear that the values of stress as well as flow laws that are measured with this technique are consistent with measured values that come from more traditional techniques. The ability to resolve time in the low temperature range of these measurements adds a significant dimension to results provided by standard indentation experiments.

2.3. Macro-scale stress

It is possible to generate non-hydrostatic stress that is uniform over the dimension of the X-ray scattering volume, by introducing hard end plugs above and below the sample chamber. The anisotropy of the cell is thus, responsible for causing deviatoric stress in the sample. For the X-ray diffraction vector parallel to the cylinder axis (as in the DIA apparatus), a stress field with a cylindrical symmetry does not broaden the diffraction peaks, but displaces the peaks by differing amounts. The displacement of each peak depends on the magnitude of the stress field and the elastic moduli of the sample (see discussions by Kinsland and Bassett, 1977; Singh and Kennedy, 1974; Singh, 1993; Singh and Balasingh, 1994; Weidner et al., 1992b, 1994, 1998; Weidner, 1998).

In order to measure rheological properties, strain metrics are needed to monitor plastic strain of the sample as a function of time. Monitoring of sample length or strain markers such as that used by Karato and Rubie (1997) hold a possible application for in situ, time-dependent stress–strain determinations. We have conducted a study on an MgO sample using X-ray shadowgraphs that demonstrate the feasibility of doing this during a high pressure–high temperature experiment. The cell was constructed to have a very hard axial direction, with the sample sandwiched between two corundum pistons. A thin gold foil was placed at each end of the sintered MgO sample. X-rays that bathe the sample were converted to visible light by a fluorescence screen down-stream of the sample. This

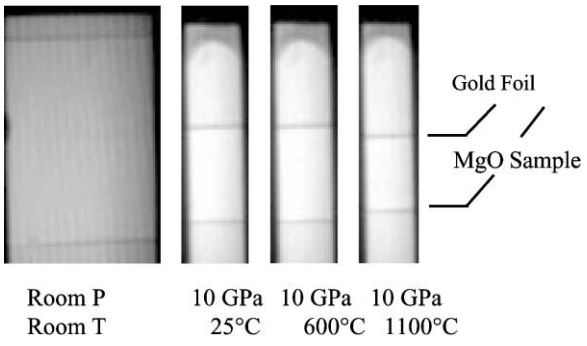

Fig. 9. X-ray shadowgraph of MgO sample at different *P*–*T*–time conditions. Horizontal lines are due to gold foils placed at top and bottom of sample. The width of the shadowgraph is defined by the opening between anvils.

image was magnified and recorded on videotape. A typical image is displayed in Fig. 9. The two dark lines are from the gold foil at the top and bottom of the sample while the width of the illuminated region is determined by the size of the gap between the anvils. Captured digital images were analyzed to determine length, strain, and strain rate. Length as a function of time is illustrated in Fig. 10 in units of pixels, where one pixel is about 4 μm. The regions with no data were periods when the X-rays were used for diffraction. The sample was compressed during the first 150 min of the experiment. During this time, the length was reduced to half of its initial value. At the final pressure, the sample was heated to 600°C at the 210 min point and held until the 300 min point, when it was further heated to 1100°C. Both heating cycles evidenced a further shortening even though no further loading of the press occurred. Thus, differential stress was maintained in the sample and assembly throughout the experiment. Fig. 11 shows the strain rate after the temperature increases from 600 to 1100°C. In this experiment, we estimate an uncertainty in strain of 0.001. Recent improvements in the camera system have improved the resolution to 0.0001 for samples of 1 mm length.

The X-ray diffraction pattern has the possibility to determine the time dependence of many aspects of the experiment. For example, peak heights are sensitive to any preferred orientations that develop within the sample. For the MgO sample reported here, a strong lattice preferred orientation developed during cold compression as shown by the X-ray intensities of Fig. 12. The top and bottom of the sample demonstrate unusually small intensities in the (2 0 0) and (4 0 0) peaks compared to the (1 1 1), (2 2 0), and (2 2 2) peaks, while in the center, the reverse is true. This suggests that dislocation flow was responsible for a significant amount of the shortening as the equant-shaped grains should not develop a fabric if the flow occurred by rotation. Furthermore, the orientations of the finite strain ellipses and hence the flow lines vary with position in the sample. Once in place, the fabric remained throughout the experiment.

The magnitude of the deviatoric stress may be determined from the elastic strain recorded by individual

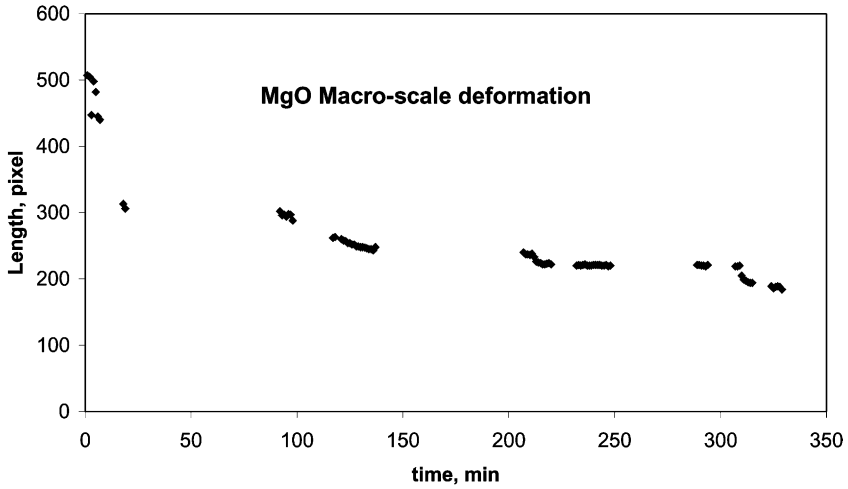

Fig. 10. Length of MgO sample as a function of time measured in pixels (~4 μm) of digital image.

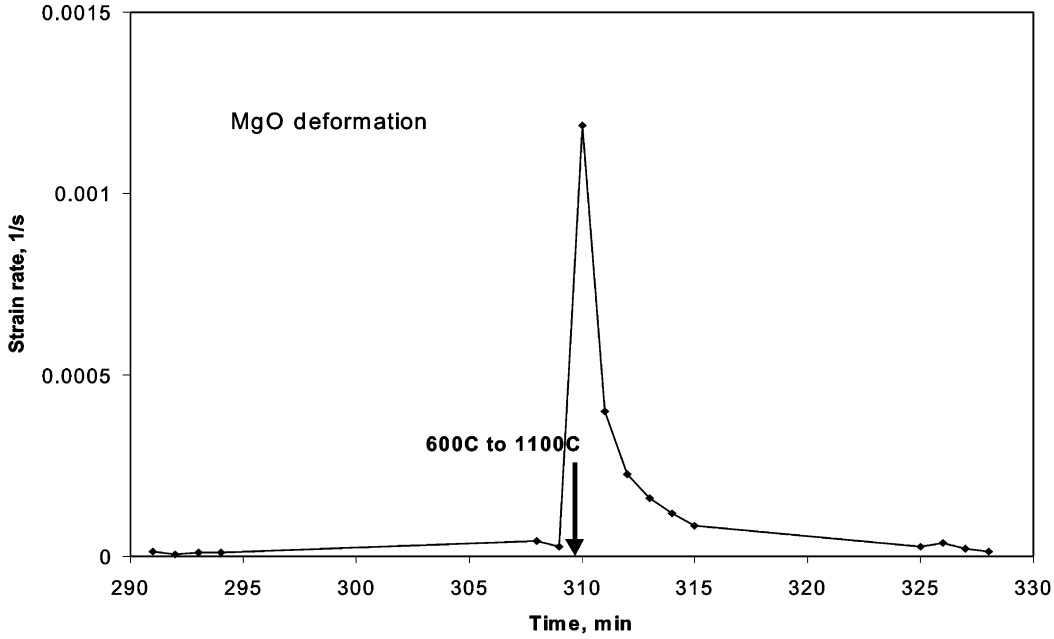

Fig. 11. Strain rate as a function of time of MgO sample determined from digital images as the temperature is increased from 600 to 1100°C.

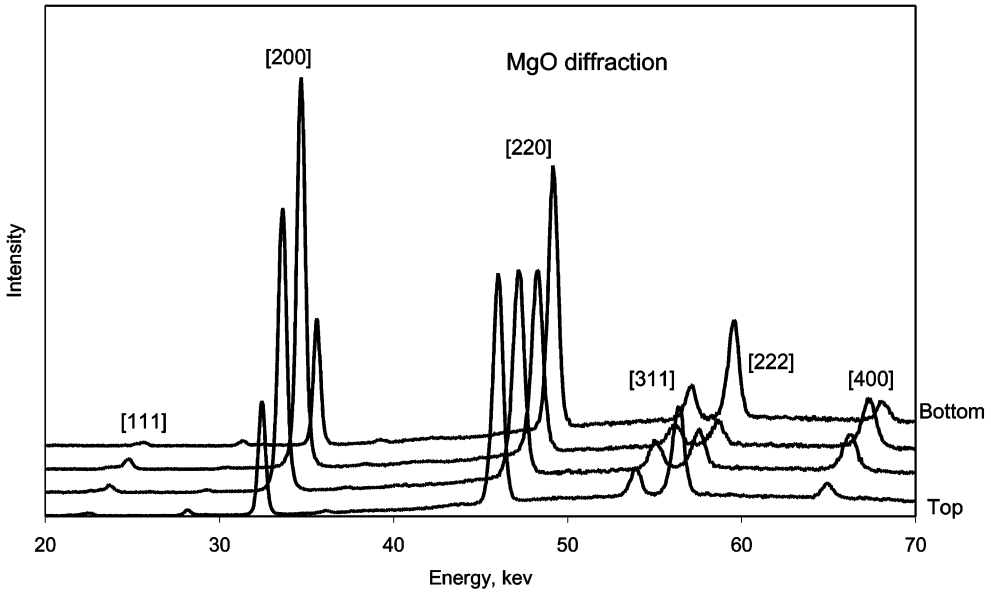

Fig. 12. X-ray diffraction patterns measured along the length of the MgO sample during cold compression. The patterns have been displaced along both axes to aid the viewing of the signals.

diffraction peaks ($h\,k\,l$), as is given by

$$\varepsilon_{(h\,k\,l)} = \frac{\Delta d_{(h\,k\,l)}}{d_{(h\,k\,l)}} = S_{11}\sigma_1 + (S_{12} + S_{13})\sigma_3 \qquad (4)$$

where the compliance tensor, S, is rotated to the coordinate system of the stress system. The important point here is that each peak is generated from a subset of the crystals in the sample. This subset are all oriented with the particular crystallographic axis, ($h\,k\,l$), parallel to the diffraction vector, which in our case is also the maximum stress axis. Since each peak corresponds to a different orientation, the values of the Ss will change with ($h\,k\,l$). However, the magnitude of the variation of the Ss with ($h\,k\,l$) depends on the elastic anisotropy of the sample. An isotropic material will have the same value of S_{ij} for all crystallographic orientations. Thus, an isotropic material will manifest strains for each diffraction peak that are shifted from the hydrostatic value, but the magnitude of the shift will be the same for each diffraction peak. A material that is elastically anisotropic, will exhibit strains that vary with orientation (or ($h\,k\,l$)), and the magnitude of the variation will be proportional to the magnitude of the differential stress.

Eq. (4) has been used to define the stress field in the case where the elastic anisotropy is known (Weidner et al., 1994) and to define the elastic properties of the material (i.e. the S_{ij}s) in the case where the stress state is defined (Mao et al., 1998). In both cases, it is assumed that the stress is uniform and does not vary with orientation of the grains. Indeed, the grains that contribute to a (2 2 2) X-ray peak do not contribute to the (2 0 0) peak, as mutually exclusive orientations are required for each peak. The local stress field is influenced by the orientation of the particular grain since some directions in the grain are stiffer than others. A Reuss type assumption would assert that each grain samples the local stress field, while a Voigt type assumption would assert that each grain samples the local strain field. The Voigt state would result in exactly the same displacement (strain) of each of the diffraction peaks and there would be no signal originating from the deviatoric stress. Eq. (4) is actually appropriate for the Reuss state. An intermediate state, such as the Hill state, would imply that the stress calculated in this equation is about a factor of 2, too small.

A more profound effect can result from an anisotropy in strength. A material that flows significantly during loading can result with stresses in individual grains that represent the strength of the individual orientation of the grain. For example, if a cubic material has a very soft slip system on (1 0 0) planes, then grains with (1 0 0) parallel to the maximum stress will support higher values of σ_1 than other grains. Thus, the elastic strain for these grains will be greater than others. Such information would be incorrectly interpreted by using the above equation.

The results for MgO include effects of anisotropic strength. Analysis of the stress field using Eq. (4) during compression yielded a tensional stress in excess of 2 GPa parallel to the cylinder axis, yet the sample shortened considerably during this phase of the experiment. Uchida et al. (1998) observed the same strain distribution for MgO, but concluded that it was due to a change in the sign of anisotropy at about 3 GPa. This conclusion is contradicted by the elastic moduli data of Chen et al. (1998a) who found very little change in elastic anisotropy to much higher pressure. The specific observation is that the (2 0 0) diffraction peak indicated a larger strain than the other peaks. This could be due to tension along the diffraction direction (high stress axis) or higher stress on grains with (1 0 0) parallel to the compression axis. The latter results if the easy slip systems are on (1 0 0) planes. Taken together with the preferred orientation, this information indicates that the low temperature flow in MgO occurred on (1 0 0) planes and that the flow directions varied between the middle and the ends of the MgO sample in this study.

On heating, the situation changed for this MgO sample. Applying Eq. (4) to the diffraction data indicated a compressive stress parallel to the shortening axis of about 1 GPa at 600°C. The most stable results were obtained using only the two strongest peaks in the diffraction pattern (2 0 0) and (2 2 0). Heating to 1100°C resulted in a decrease in the differential stress to about 0.5 GPa. In both cases, the diffraction patterns were taken about 20 min after the temperature increase when strain rate was about $10^{-5}\,s^{-1}$. Frost and Ashby (1982) estimated the differential stress to overcome obstacles to be about 1.2 GPa for MgO. Their model would suggest that obstacles should limit flow at 600°C but that power law creep may be effective by 1100°C with a differential stress of about 0.4–0.5 GPa for a strain rate of $10^{-5}\,s^{-1}$. Thus, for the elevated temperature measurements of flow in MgO,

the macro-scale stress–strain rate relation that is measured for a reference material is in excellent agreement with existing models.

Clearly there are uncertainties with the stress measurements in the macro-scale stress analysis. The approach outlined here determines this stress from diffraction data obtained at a fixed position relative to the stress axis. If the entire Debye ring can be defined, then it is much more straightforward to define the stress. Weidner (1998) demonstrate that the ellipticity of the Debye ring can yield a more robust measure of the differential stress and has fewer of the ambiguities discussed here. Our DIA geometry does not allow measurement of the full Debye ring, however, other guide-blocks and future strategies may.

3. Mantle minerals

We have carried out micro-scale stress measurements on several mantle minerals including olivine, wadsleyite, ringwoodite, majorite-rich garnet, and magnesium silicate perovskite. While many of these studies are still in progress to define the flow laws and deformation mechanisms, we will describe the relative properties here. The effect of water on the observed strength has already been presented (Chen et al., 1998b) and would not be further discussed below.

One useful measure of the mineral rheology is the 1000 s strength, that is the deviatoric stress supported by the sample upon holding temperature constant for 1000 s. In our studies, this stress is relatively independent of the time–temperature path that precede the data point as long as the stress exceeded saturation. From a flow law viewpoint, this is the stress for a strain rate of about $10^{-7}\,s^{-1}$. The 1000 s strength is illustrated in Fig. 13 for these minerals as a function of temperature. All minerals exhibit a strength of several GPa at low temperatures and a thermally induced softening at higher temperatures which is probably the result of a thermally activated process. The temperature for this process is lowest for olivine for which it is about 500°C. Wadsleyite and majorite soften at about 700°C, and ringwoodite softens at a slightly higher temperature. We did not observe a significant thermal softening of perovskite in the experimental range, which extended to 800°C.

The point of thermal softening is still not in the power law creep regime, because the effective n is well above 5 for all of these materials. Thus, we conclude

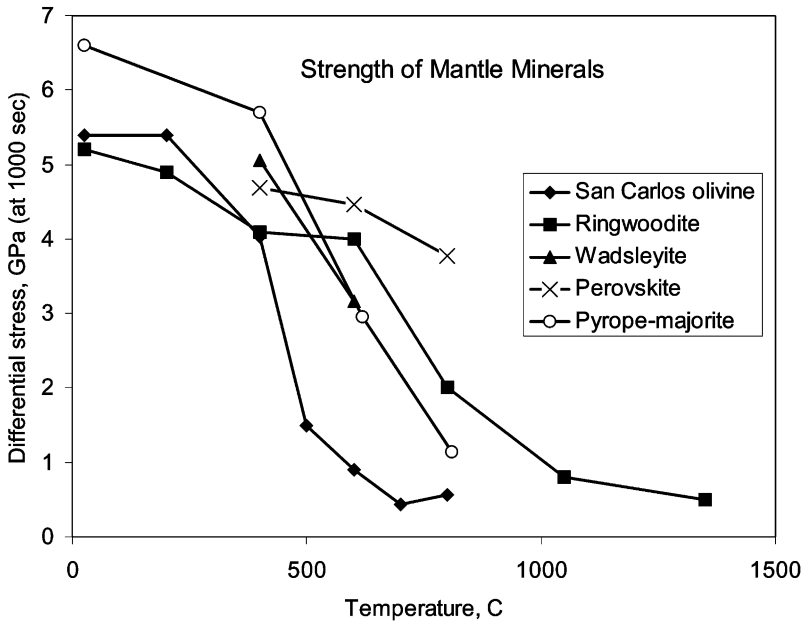

Fig. 13. The 1000 s strength of mantle minerals as a function of temperature. This is the measured differential stress that can be supported during a relaxation experiment 1000 s after the initial load was applied.

that this region generally corresponds to glide or to a transition region between glide and climb. Temperatures above the softening region may well correspond to power law creep.

The picture that emerges includes three thermally defined regions. The low temperature region exhibits a strength of several GPa, which is relatively temperature independent. Strain rate depends strongly on stress. For stress higher than the 1000 s strength, strain rate becomes very fast, yet for lower stresses, the strain rate is quite slow. Expressed as a power law flow law, the effective value of n is often above 20. The softening region is characterized by a strong temperature dependence of strength, with an effective n still greater than that expected in the normal power law creep regime. The high temperature region demonstrates a reduced temperature dependence of strength and less dependence of strain rate on stress. Values of n are often in the range of 3–5.

The thermal softening region has important rheological characteristics that may have a bearing on the deep earthquake process. Ogawa (1987) and Hobbs and Ord (1988) demonstrate that a plastic instability mechanism for deep earthquakes requires a rheology with a strong stress and temperature dependence. This is precisely the characteristic of the softening region that is identified by our data. At lower temperatures, the stress dependence of the strain rate is high, but the temperature dependence is low. Thus, softening due to flow-induced heating will not be so significant. At higher temperatures, the stress dependence diminishes, reducing the effect of stress concentrations at the 'crack' tip.

Elevated temperatures will eventually cause seismicity to cease as there is insufficient strength to support seismogenic stresses for sufficient times. Holt (1995) and Bevis (1988) estimate a strain rate of $10^{-15}\,s^{-1}$ for the flow process that results from deep earthquakes. If creep becomes sufficiently active that it exceeds this flow rate, then we would expect that deep seismicity would shut off since plastic flow will drain stress from the region more efficiently than seismic activity. Using the power law creep law of Hirth and Kohlstedt (1996), we estimate that for 100 MPa

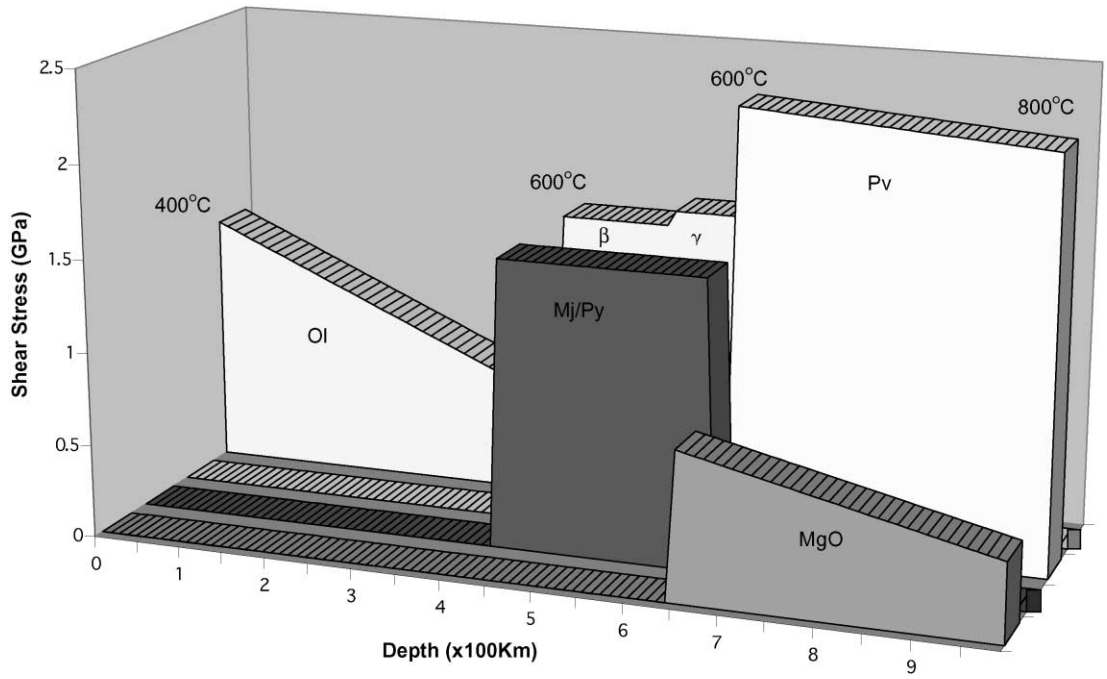

Fig. 14. Stress capacity of the subduction zone. The 1000 s strength is projected along a geotherm in the cold center of a subducting slab. Phase transformations give rise to sudden increases in strength at the appropriate depths.

of shear stress, creep will shut down the seismic process at 600°C in wet olivine (their preferred oceanic lithosphere model) and at 700°C for dry olivine. Thus, we expect that such temperatures represent a maximum temperature for seismicity above 400 km where olivine is the stable mineral.

A plastic instability origin of deep earthquakes is consistent with many of the depth variations in seismic character. The decrease in seismicity from 350 to 400 km could reflect the approach of the temperature to 600°C in the bulk of the slab by this depth. The increase in seismicity below 400 km depth reflects the higher temperature for thermal softening of the high pressure phases. Cessation of seismicity at the perovskite boundary may be a result of the strong, temperature independent nature of perovskite.

These measurements also provide important constraints on the rheology of the slab as is required for dynamic models of subduction. Fig. 14 illustrates the stress capacity of the subduction region along the cold center of the slab. Again, the 1000 s strength is illustrated. Phase transitions mark strong increases in strength as is illustrated here, with the perovskite region being extremely strong. We do not account for secondary phases. In the upper mantle and transition zone, they should be as strong as those that are represented here. In the lower mantle, we expect up to 15% magnesiowustite in addition to perovskite, which might weaken the slab. However, the amount of weakening will depend on the distribution of the magnesiowustite. Further experiments will define the flow laws of these materials.

4. Conclusion

Credible stress–strain rate relations are defined by synchrotron-based measurements. Micro-scale stress measurements are based on relating deviatoric stress to stress heterogeneities. The stress field is created as a powdered sample is compressed and is expressed as a broadening of the X-ray diffraction peak. Relaxation of the stress field can be observed with time resolved X-ray diffraction. The time dependence enables an empirical flow law to be defined. Literature data agree with the empirical flow laws for spinel, corundum, and olivine in the temperature regime reported here. Generally, these measurements have been limited to deviatoric stresses greater than about 100 MPa. This has allowed analyses of only a small region of parameter space where the defining flow regime is the high-temperature power law creep regime. However, the lower temperature regimes probably control flow in the cold part of a subducting slab.

Preliminary data are presented for most phases that exist within a subducting slab. Higher pressure phases tend to be stronger at elevated temperatures. In particular, thermal activation of the weakening process occurs at higher temperatures for the higher pressure phases. Association of the seismogenic zone with the temperature regime where strength is a strong function of temperature suggests that earthquakes in high pressure phases occur at higher temperatures than those in olivine. In fact, olivine probably becomes too weak to support earthquakes at temperatures in excess of 600–700°C. Thus, the decrease in seismicity with depth to 400 km may result from the weakening of olivine in the slab at these depths. The increase in seismicity deeper than 400 km would then result from the increased strength of the higher pressure phases. The disappearance of earthquakes in the perovskite field may reflect the loss of a plastic instability mechanism associated with the rheology of perovskite. More experiments are required to verify this possibility.

Acknowledgements

Part of this research was conducted at the National Synchrotron Light Source X17B of Brookhaven National Lab and at the Advanced Photon Source, GSECARS beamline, Argonne National Lab. Jerry Hastings, Yanbin Wang, and Mark Rivers, at these facilities were instrumental in the success of this research. Support was provided by NSF through CHiPR and EAR9909266.

References

Ando, K., Oishi, Y., 1974. J. Chem. Phys. 61, 625.

Bevis, M., 1988. Seismic slip and down-dip strain rates in Wadati–Benioff zones. Science 240, 1317–1319.

Chen, G., Liebermann, R.C., Weidner, D.J., 1998a. Single-crystal MgO to 8 GPa and 1600 K. Science 280, 1913–1916.

Chen, J., Inoue, T., Weidner, D.J., Wu, Y., Vaughan, M.T., 1998b. Strength and water weakening of mantle minerals, olivine,

wadsleyite, and ringwoodite. Geophys. Res. Lett. 25, 575–578 and 1103–1104.

Choi, D.M., 1965. PhD thesis. North Carolina State University at Raleigh.

Evans, B., Goetze, C., 1979. The temperature variation of hardness of olivine and its implication for polycrystalline yield stress. J. Geophys. Res. 84, 5505–5524.

Frost, H.J., Ashby, M.F., 1982. Deformation-Mechanism Maps, The Plasticity and Creep of Metals and Ceramics. Pergamon Press, Oxford, 166 p.

Goetze, C., 1978. The mechanisms of creep in olivine. Philos. Trans. R. Soc. London A 288, 99–119.

Hirth, G., Kohlstedt, D.L., 1996. Water in the oceanic upper mantle implications for rheology, melt extraction and the evolution of the lithosphere. Earth Planet. Sci. Lett. 144, 93–108.

Hobbs, B.E., Ord, A., 1988. Plastic instabilities: implications for the origin of intermediate and deep earthquakes. J. Geophys. Res. 93, 10521–10540.

Holt, W.E., 1995. Flow fields within the Tonga slab determined form the moment tensors of deep earthquakes. Geophys. Res. Lett. 22, 989–992.

Karato, S.I., Rubie, D.C., 1997. Toward an experimental study of deep mantle rheology a new multi-anvil sample assembly for deformation studies under high pressures and temperatures. J. Geophys. Res. 102, 20111–20122.

Kinsland, G.L., Bassett, W., 1977. Strength of MgO and NaCl polycrystals to confining pressures of 250 Kbar at 25°C. J. Appl. Phys. 48, 978–985.

Mao, H.K. et al., 1998. Elasticity and rheology of iron above 200 GPa and the nature of the earth's inner core, Nature, 396, 741–743.

Meade, C., Jeanloz, R., 1990. The strength of mantle silicates at high pressures and room temperature: implications for the viscosity of the mantle. Nature 348, 533–535.

Ogawa, M., 1987. Shear instability in a viscoelastic material as the cause of deep focus earthquakes. J. Geophys. Res. 92, 13801–13810.

Phakey, P., Dollinger, G., Christie, J., 1972. Transmission electron microscopy of experimentally deformed olivine crystals in flow and fracture of rocks. In: Heard, H.C., Borg, I.Y., Carter, N.L., Raleigh, C.B. (Eds.), Flow and Fracture of Rocks. Geophysical Monograph. American Geophysical Union, Washington, DC.

Singh, A.K., 1993. The lattice strains in a specimen (cubic symmetry) compressed non-hydrostatically in an opposed anvil device. J. Appl. Phys. 73, 4278–4286.

Singh, A.K., Balasingh, C., 1994. The lattice strains in a specimen (hexagonal system) compressed non-hydrostatically in an opposed anvil high pressure setup. J. Appl. Phys. 75 (10), 4956–4962.

Singh, A.K., Kennedy, G.C., 1974. Uniaxial stress component in tungsten carbide anvil high-pressure X-ray cameras. J. Appl. Phys. 45 (11), 4686–4691.

Uchida, T., Yagi, T., Katsuya, O., Funamori, N., 1998. Analysis of powder X-ray diffraction data obtained under uniaxial stress field. Rev. High Pressure Sci. Technol. 7, 269–271.

Vaughan, M.T. et al., 1998. T-cup: a new high-pressure apparatus for X-ray studies. Rev. High Pressure Sci. Technol. 7, 1520–1522.

Weidner, D.J., 1998. Rheological studies at high pressure. In: Ribbe, P.H. (Ed.), Reviews in Mineralogy. I. Ultrahigh-pressure Mineralogy: Physics and Chemistry of the Earth's Deep Interior. Mineralogical Society of America, Washington, DC, pp. 493–524.

Weidner, D.J., et al., 1992a. Large volume high pressure research using the wiggler port at NSLS. High Pressure Res. 8, 617–623.

Weidner, D.J., et al., 1992b. Characterization of stress, pressure, and temperature in SAM85: a DIA type high pressure apparatus. In: Syono, Y., Manghnani, M.H. (Eds.), High-pressure Research: Application to Earth and Planetary Sciences. Terra Scientific Publishing Company and American Geophysical Union, Tokyo and Washington, DC, pp. 13–17.

Weidner, D.J., Wang, Y., Vaughan, M.T., 1994. Deviatoric stress measurements at high pressure and temperature. In: Schmidt, S.C., Shaner, J.W., Samara, G.A., Ross, M. (Eds.), High-pressure Science and Technology. Proceedings of the 1993 AIRAPT Conference, pp. 1025–1028.

Weidner, D.J., Wang, Y.B., Chen, G., Ando, J., 1998. Rheology measurements at high pressure and temperature. In: Manghnani, M.H., Yagi, T. (Eds.), Properties of Earth and Planetary Materials at High Pressure and Temperature. Geophysical Monograph. American Geophysical Union, Washington, DC, pp. 473–480.

Westbrook, J.H., 1966. Rev. Hautes Temper. et Refract. 3, 47.